

# A compact study on impact of multiplicative *Streblus asper* inspired biogenic silver nanoparticles as effective photocatalyst, good antibacterial agent and interplay upon interaction with human serum albumin

Somnath Das, Arindam Das, Anukul Maji, Maidul Beg, Anindita Singha, Maidul Hossain\*

Department of Chemistry and Chemical Technology, Vidyasagar University, Midnapore 721 102, West Bengal, India

## ARTICLE INFO

### Article history:

Received 5 February 2018

Received in revised form 21 February 2018

Accepted 24 February 2018

Available online xxx

### Keywords:

Silver nanoparticles

Green synthesis

Photocatalytic activity

HSA interaction

XRD analysis

CD spectroscopy

Fluorescence lifetime

## ABSTRACT

Chemical stabilized nanomaterials have enjoyed success as multifunctional therapeutic, diagnostic, catalytic properties and resolved a number of issues associated on interaction with biological systems. But they are unable to conquer the pricey synthetic route and production of chemical hazards. To triumph over this inadequacy, a one-step economically benign cost-effective synthesis of silver nanoparticles from a renewable plant, *S. asper*, was proclaimed and its infliction on photocatalytic efficiency, antibacterial activity and interaction with human serum albumin (HSA) was described. The characterization of nanoparticles was well esteemed by UV-vis, DLS, HR-TEM, FE-SEM, XRD, FT-IR and zeta potential assessment. The degree of crystallinity and size of the synthesized nanoparticles obtained from HR-TEM (~13 nm) was convincingly commensurate the XRD data. The nanoparticles effectively fascinate the degradation of toxic phenothiazinium dye methylene blue and anthropogenic contaminant 4-nitrophenol in a short course time. The nanoparticles were revealed good antibacterial activity against *Escherichia coli* ATCC 25922. Due to limited understanding of protein-nanoparticles associated outcome, the study on the interaction of nanoparticles is very decisive on investigating interactions with specific biological systems. Thus, in order to explicit the protein-nanoparticles binding utility to a high resolution, herein we demonstrate the interaction study of HSA with *S. asper* stabilized silver nanoparticles (SNPs). Absorption, fluorescence spectroscopic studies exhibit the existence of  $\sim 10^8$  orders binding upon interaction. Thermodynamic parameter ( $\Delta G$ ) indicated that the process was spontaneous. The fluorescence lifetime measurement revealed the subsistence of static binding mechanism, evolves via ground state HSA-SNPs binary complex formation. CD spectral study explored upon interaction protein structure was unaltered with slight decrement in  $\alpha$ -helix content (56.2% to 52.9%). High negative zeta potential of HSA-SNPs (-49.4 mV) complex compared to SNPs (-25.3 mV) substantiated the stabilization of HSA-SNPs complex with the formation of protein on the nanoparticles surface.

© 2017.

## 1. Introduction

Nano-biotechnology is the crush of nanotechnology and biotechnology. In last two years, nano-biotechnology has sparked scientific research towards a rapidly growing interest due to its large promising socioeconomic impact of producing and utilizing nano-sized particles. The emerging advance of this field is to fascinate the efficacy of nano-sized structures for highly updated and improved biotechnology. At the present time, a most popular research platform in this field is the synthesis of nanoparticles (NPs) which have gained ample attention because of their special functional properties for several applications in fuel cells, luminescence tagging, imaging, multiplexing biomedical applications, diagnostics and most recently biosensors [1–6]. Among the numerous noble metal nanoparticles silver nanoparticles (AgNPs) have provoked great attention due to their diverse superior properties in different fields, for instance, medical, cosmetics, pharmaceutical agriculture, antifungal activities, improved antimicro-

bial, enhanced catalytic and optical properties sensors, bio-labeling, filters, and drug delivery system [7–9].

In very recent reports, Das et al. have developed 5-sulfosalicylic acid modified novel silver nanoparticles for detection of hazardous pollutant mercuric ion and sulfide ion at ultra trace nM level [10]. Similarly, Beytur et al. have reported a tremendous efficient voltammetric sensor developed by polymer directed Ag@Au NPs ionic liquid improved glassy carbon electrode for selective detection of a vital cephalosporin antibiotic ceftizoxime which was found very efficient in real pharmaceutical samples for ceftizoxime analysis [11]. Atar et al. reported the Fe@Ag NPs/2-aminoethanethiol modified graphene oxide composite and showed its efficient application in lithium-ion batteries as a better anode material [12]. Yola et al. produced a composite of colemanite and silver nanoparticles, was found an effective photocatalyst [13] and Atar et al. developed an electrocatalyst for methanol oxidation directed by silver nanoparticles [14]. Thus, the nature of applicative response for each NP varies on their way of synthesis. There are numerous technical methods such as chemical reduction [15]; thermal decomposition [16], photoreduction [17], ion sputtering [18], and sol gel [19] in reverse micelles have been pub-

\* Corresponding author.

Email address: hossainm@mail.vidyasagar.ac.in (M. Hossain)

lished by scientific journals. Unfortunately, most of these methods are extremely expensive and required hazardous reagents, high energy reaction condition or involve the use of a lot of organic solvents which needs rather difficult wasteful purification [20]. Thus, a scenario clearly shows that whatever the method followed, all these synthetic techniques must bear a probability of chemical contamination which may pose potential, biological and environmental risks. Therefore, it is very much crucial to replace these expensive non-biocompatible and classical synthetic protocols by simple, economic and biocompatible methods, which is commercially economic, viable as well as environmentally compatible. In that filed green synthesis of AgNPs have attracted merit importance due to its one-step, faster, cost-effective, nontoxic and eco-friendly synthetic approach. There are several green methods for preparation of AgNPs by using bacteria, fungi, actinomycetes, algae, virus, leaf extract, root extract, bulb and latex of plant, biological material such as honey, starch, ascorbic acid etc. [21–23]. Displaying the aesthetic sense, the plant-mediated syntheses are rendering themselves as key procedure and proving their potential at the top. A literature survey revealed that plant-mediated AgNPs were used in the different area of industries, medicine, packaging, animal husbandry, military, cosmetics, and health [24–26].

In spite of this, there is not much knowledge that is known about the effect of such nanoscale particles on biological system and their potential toxicity on the living system [27–29]. The effect of NPs inside the body may have diverse effects on the conformation of normal protein function or can expose new epitopes on the protein surface [30]. This could provoke some uncertain biological disordered reactions and lead to toxicity.

On the other hand, AgNPs also have engrossed remarkable attention for their sharp electrical properties and distinctive optical signature due to high molar extinction coefficient. This inherent optical property and high surface area of AgNPs makes it compatible with the photocatalytic application. At present time, enhanced photocatalytic property for degradation of organic dye by using green synthesized AgNPs is a most popular topic [31]. A lot of published article highlighted AgNPs mediated removal of the organic dye is a better alternative way than electro-coagulation [32], redox treatment [33] and carbon sorption [34,35] type common methods. Thus, AgNPs can singly act as a multi-applicative economic weapon for developing alternative low-cost adorable methods for several important applications. Therefore, plant-mediated synthesis of AgNPs has received much attention of the scientists to better understand the idea of protein-NP interactions to a higher impact and development of eco-friendly alternative methods for biological implications [36].

Human serum albumin (HSA) is one most abundant protein subsistent in human blood plasma. It constitutes about half of serum protein and acts as a transporter of fatty acids, hormones, and other compounds. HSA has three homologous domains (namely I, II, and III) bring together to form a heart shaped globular protein (Mol wt. 66 kDa, consists of 585 amino acids) and has many physiological functions. Crystallographic studies revealed that the protein has two principle ligand binding sites called sites I (located within sub-II A) and site II (located in sub III). The structure and functions of active sites of HSA can modify upon interaction with molecules, which in turn may lead to several important or detrimental effects. However, there are very few reports on the interaction between HSA and plant mediated silver nanoparticles [37] but our ongoing research was fully highlighted on this and several papers have been published [38–40].

*Streblus asper* Lour found in tropical countries such as India, Malaysia, Philippines and Thailand (common names are siora (Hindi), Sheora (Bengali), piray (Tamil) etc.) It is traditionally used in Ayurveda and folk medicine [41]. *Streblus asper* Lour plant leaves

show several biodiverse application on treating cardiotoxic activity, anti-filarial activity, anticancer activity, antimicrobial activity, anti-allergic activity, insecticidal activity, anti-parasitic activity have been reported [42,43].

Herein, in an attempt, we inaugurate an eco-friendly and very short synthetic route for the preparation of biogenic silver nanoparticles by using *Streblus asper* Lour leaves extract (served as both reducing and stabilizing agent) at room temperature. On remembering the impact of *Streblus asper*, we have studied the activity of synthesized silver nanoparticles into three different application fields and for the first time, we report it in a single article. Firstly, in order to resolve the photocatalytic activity; the efficiency of prepared nanoparticles were investigated on degrading toxic phenothiazinium dye methylene blue and reduction of 4-nitrophenol under solar radiation. Secondly, a study was done to understand the efficacy of AgNPs against a gram-negative bacterium (*E. coli* ATCC 25922). Further, the synergistic antibacterial activity of synthesized biogenic AgNPs at its LD<sub>50</sub> dosage in combination with ampicillin (an antibiotic) against the test strain was researched. Lastly, we have focused our study on the interaction of biogenic AgNPs with HSA by a spectroscopic approach to better understand the biophysical binding mechanism and stabilization function parameters upon interaction with protein in more detail.

## 2. Experimental section

### 2.1. Chemicals and reagents

All the used chemicals were analytical reagent grade and Millipore water was used for overall work done. Silver nitrate (AgNO<sub>3</sub>, 99.99%) was buying from Merck (Darmstadt, Germany, <http://www.merck.com>). *Streblus asper* leaf was collected from Dsagram, Sabang, West Bengal, India. Methylene blue (MB), human serum albumin (HSA), 4-nitrophenol (4-NP) and sodium borohydride (NaBH<sub>4</sub>) were purchased from Sigma–Aldrich (<https://www.sigmaaldrich.com>). HSA sample was prepared in 10 mM citrate-phosphate buffer (CP) at pH 7.05. The concentration of HSA and methylene blue (MB) were determined by using molar extinction coefficients values 35,700 M<sup>-1</sup> cm<sup>-1</sup> at 280 nm and 76,000 M<sup>-1</sup> cm<sup>-1</sup> at 664 nm. All the apparatus were properly cleaned by aqua-regia and followed by distilled water prior to use.

### 2.2. Instruments used

Absorption and fluorescence spectral measurement were experimented by Shimadzu Pharmaspec-1601 unit (Shimadzu Corporation, Kyoto, Japan) and Hitachi F-7000 (Hitachi Ltd., Tokyo, Japan) respectively. Fluorescence decay profile measurements were estimated with a Horiba Jobin Yvon Fluoro Max (Horiba Jobin Yvon, Glasgow, UK) using the time-correlated single photon counting (TCSPC) technique (scattering was measured by using a Ludox solution, excitation was performed at 288 nm with a delta diode-C1 diode controller). Hydrodynamic size (final data were taken after averaging 30 scans) of the nanoparticle and zeta measurement was measured by Zetasizer Nano ZS instrument (Malvern Instrument, Malvern, Worcestershire, UK) ZS with 633 nm He–Ne laser, fitted with an MPT-2 Autotitrator. The zeta potential and dynamic light scattering (DLS) of each sample were computed using the software provided by the attached unit. FT-IR spectra were quantitatively checked after background correction (averaging 50 scans for each) using a Perkin-Elmer Spectrum two FT-IR spectrophotometer equipped with a zinc selenide (ZnSe) attenuated total reflectance (ATR) accessory, LiTaO<sub>3</sub> detector, and a KBr

beam splitter at room temperature (Perkin Elmer, Inc., USA). X-Ray Diffraction (XRD) pattern was recorded by Bruker D8 Discover Davinci System (Detector: Lynxeye (1-dimensional silicon strip technology Detector)) (Target: Cu). Field Emission Electron Microscope (FE-SEM), Carl Zeiss SMT AG (Germany) electron microscope operating at 5 kV was used for nanoparticles characterization. TEM images were taken by JEM-2100 High-Resolution Transmission Electron Microscope (HR-TEM) (JEOL Ltd., 1-2, Musashino 3-Chome, Akishima, Tokyo 196-8558, Japan, <http://www.jeol.co.jp>) operating at 200 kV was used to determine the exact morphology of synthesized nanoparticles. The average particle size was determined by Image J software (version 1.45S). The elemental estimation (present in the nanoparticles) was analyzed by energy dispersive X-ray (EDX) spectrometer. Circular dichroism (CD) spectra were recorded on a PC-driven Jasco J815 spectropolarimeter (JASCO International Co, Ltd., Tokyo, Japan) attached to a Peltier-controlled cell holder and temperature controller PFD 425 L/15 in rectangular quartz cuvettes 0.1 cm path length.

### 2.3. Preparation of leaf extract

In order to synthesize silver nanoparticles, we have prepared *S. asper* leaf extract as follows. *S. asper* leaf extract is used to prepare silver nanoparticles on the basis of cost-effectiveness, ease of availability and its medicinal property. Healthy and fresh leaves of *S. asper* were collected. Leaf surface cleaned with running tap water to remove debris and other contaminated organic contents, followed by double distilled water and air dried at room temperature. About 10 g of finely cut leaves were kept in a beaker containing 100 ml Millipore water and heated up to boil at 80 °C with continuous stirring at 450 rpm for 1 h. The extract was cooled down and filtered. The greenish yellow color filtrate was the *S. asper* leaf extract (SAE) and stored at 4 °C in the sealed tube prior to use.

### 2.4. Green synthesis silver nanoparticles

Biosynthesis of silver nanoparticles was conducted after preparation of SAE and the description of synthesis procedure is as follows: 10 mL solution of SAE was added to 2 mM solution of AgNO<sub>3</sub> under stirring condition at room temperature. The total volume of the reaction mixture was 100 mL. After 30 min the reduction of Ag<sup>+</sup> ion was started, confirmed by the appearance of red-brown color from a light greenish yellow color SAE solution which indicated the nanoparticles formation. In an attempt to complete the reduction of Ag<sup>+</sup> ions by SAE, the stirring was continued up to 3 h. The red-brown color solution was then centrifuged at 13,500 rpm for 5 min at room temperature. After that obtained supernatant was discarded and the precipitation was resuspended in Millipore water (the process is continued for three times for purification). Finally, the stable prominent red-brown color solution was the purified *S. asper* stabilized AgNPs (SNPs) and was used for characterization.

### 2.5. Concentration assessment of *S. asper* stabilized AgNPs (SNPs)

On the basis of the size of SNPs (obtained from HR-TEM), the concentration of SNPs was determined by UV–vis spectroscopy based on a molar extinction coefficient  $17,308 \times 10^5 \text{ M}^{-1} \text{ cm}^{-1}$  at a wavelength of 425 nm (Mie theory based) [44]. The final concentration of the SNPs was found  $2.9 \times 10^{-8} \text{ M}$ .

### 2.6. Photocatalytic activity of SNPs

The catalytic response of synthesized SNPs was checked for the reduction of 4-NP and degradation of MB. The study of dye degradation (for MB) and catalytic reduction reactions (for 4-NP) were carefully measured by absorbance spectrometer.

#### 2.6.1. Study of catalytic efficiency for reduction of 4-NP

In order to speculate efficacy of reduction for 4-nitrophenol to 4-aminophenol (4-AP) (by the catalytic influence of SNPs), the photocatalytic experiment was performed. In a typical experiment, 0.5 mM 4-NP and 0.02 M NaBH<sub>4</sub> solution were mixed in the 2 mL cuvette, investigated by UV–vis spectroscopy. In the same solution 10 μL (0.14 nM) synthesized SNPs were augmented and absorbance spectral changes were recorded at different time interval.

#### 2.6.2. Photocatalytic degradation of methylene blue (MB) dye

The photocatalytic degradation efficiency of SNPs for the reduction of MB was also investigated by measuring the absorbance of the UV irradiated solution of MB. Initially, the absorbance spectra of MB (5 μM) was measured. After that, 10 μL (0.14 nM) of SNPs was added to the same solution (the homogeneity of the mixture was maintained by magnetic stirring) and then exposure to UV light irradiation chamber. The regular degradation spectra of MB were recorded and at the same time, a control MB solution was also studied without the addition of AgNPs.

### 2.7. Antibacterial study

#### 2.7.1. Bacterial growth conditions and MIC determination

*Escherichia coli* (*E. coli* ATCC 25922) had been cultivated in Mueller–Hinton (MH) broth (M 391 Himedia, Mumbai, India) at 37 °C prior to utilizing. This bacterial growth condition was stored in MH broth at –70 °C supplemented with 40% glycerol.

MIC (minimum inhibitory concentration) i.e. microtiter dilution plate quantitative method [45] was employed for evaluation of the antibacterial activity of the silver nanoparticles against *E. coli* ATCC 25922. The concentration of silver nanoparticles that entirely inhibits the growth of bacterial strains is known as MIC. MIC of silver nanoparticles was determined by testing 96-well sterile microplates. Homogeneous solutions of freshly silver nanoparticles with concentration 0.25, 0.5, 1.0, 2.0, 4.0 nM in Millipore water were prepared using an ultrasonic vibrator (30 kHz, 100 W) for 10 min. 10 μL of exponentially grown cells of *E. coli* was inoculated in freshly primed 100 mL MH broth equipped with silver nanoparticles at different concentration those were early prepared and incubated at 37 °C [38–40]. The optical density of silver nanoparticles was measured at 600 nm with different time intervals of the bacterial population for determination of MIC. LD<sub>50</sub> i.e. the dose of silver nanoparticles that will cause reduction of the bacterial population to 50% was also evaluated. The average value was reported from triplicate of each experiment.

#### 2.8. Interaction study with human serum protein (HSA)

All the interaction study was carried out in 10 mM citrate-phosphate (CP) buffer (pH=7.05) at room temperature. The buffer solution was filtered through a 0.45 μm Millipore Millex-HV PVDF filter. Solid HSA was dissolved in CP buffer and concentration was measured. Interaction studies were characterized by UV–visible, fluorescence, time resolved emission and CD spectroscopy experiments.

### 3. Results and discussion

#### 3.1. Characterization of SSA-AgNPs

Initially, the formation of biogenic SNPs was well assigned from the UV-vis spectral measurement (in the range 300 nm to 700 nm) and found strong SPR (Surface Plasmon Resonance) band at 425 nm (Fig. S1). The assessment of average hydrodynamic revealed from DLS experiment was ~15 nm (Fig. S2). The characterization of morphological properties of SNPs was successively established from HR-TEM (Fig. 1A) and FE-SEM (Fig. S3) analysis. The outcome of the experimental result confirmed the formation of almost round shaped nanoparticles with a smooth surface morphology. The average size of SNPs was ~13 nm (measured from HR-TEM and histogram plot, Fig. 1B). However, slight variation in HR-TEM and DLS result in determining the average particle size endorsed because of the fact that HR-TEM quantitatively estimates the particle size of the nanoparticles in dry condition. However, the measurement of hydrodynamic radii of nanoparticles in solution was obtained from DLS experiment. We have performed EDX treatment of synthesized nanoparticles which evidenced the formation of 100% metallic silver (Fig. 1C).

FT-IR experiment was performed to prove the chief role of plant extract in stabilizing and reducing  $\text{Ag}^+$  to  $\text{Ag}^0$ . Fig. 2A and B represent IR spectrum of *S. asper* leaf extract and evidence of synthesized nanoparticles formation. The functional groups of phytochemical contents (present in the crude aqueous extract) exhibited characteristic bands at  $3632\text{ cm}^{-1}$  (—OH stretch),  $2981\text{ cm}^{-1}$ ,  $2888\text{ cm}^{-1}$  (C—H stretch),  $2627\text{ cm}^{-1}$  (—CH stretch),  $1663\text{ cm}^{-1}$  (—CO stretch),

$1526\text{ cm}^{-1}$  (C—C stretch in aromatic ring),  $1375\text{ cm}^{-1}$  (—CH rock),  $1172\text{ cm}^{-1}$  (—CO stretch),  $1064\text{ cm}^{-1}$  (C—O—C functional groups),  $910\text{ cm}^{-1}$  (—NH wagging). The compound presents in *S. asper* leaf extract (mainly phytol, lupeol, geranyl acetone, trans-Farnesyl acetate,  $\alpha$ -farnesene, betulinic acid, oleanolic acid and amino acids) were responsible for the appearance of such characteristic infrared spectral bands [43,46]. However, the FT-IR peaks position after the formation of nanoparticles were shifted towards the frequencies at  $3447\text{ cm}^{-1}$ ,  $1656\text{ cm}^{-1}$ ,  $1060\text{ cm}^{-1}$  and  $940\text{ cm}^{-1}$  (Fig. 2B) and intensity of other characteristic bands also decreased. Therefore, it can be concluded that mainly the —OH, —NH<sub>2</sub>, C=O, and C—O—C functional groups of phytochemical constituents were responsible for stabilizing as well as reducing ( $\text{Ag}^+$  to  $\text{Ag}^0$ ) in the process of SNPs formation.

#### 3.2. XRD analysis

XRD pattern of biogenic AgNPs (purified and vacuum dried) revealed instinctive diffraction patterns at  $38.10^\circ$ ,  $44.35^\circ$ ,  $64.30^\circ$ ,  $77.39^\circ$  and  $81.37^\circ$  which connects to the (111), (200), (202), (311) and (222) planes.

All these planes indicated face center cubic crystal (FCC) structure of SNPs (Fig. 3). The diffraction patterns and observed set of lattice planes values were confirmed by JCPDS file no. 96-900-8460. The sharp diffraction peaks of SNPs at respective planes confirmed the high crystalline nature and the average size was found ~13.7 nm (close to HR-TEM). To calculate the average size Debye-Scherrer formula [ $D = k\lambda/\beta_{1,2}\cos(\theta)$ ] has been used where k is the Scherrer co-

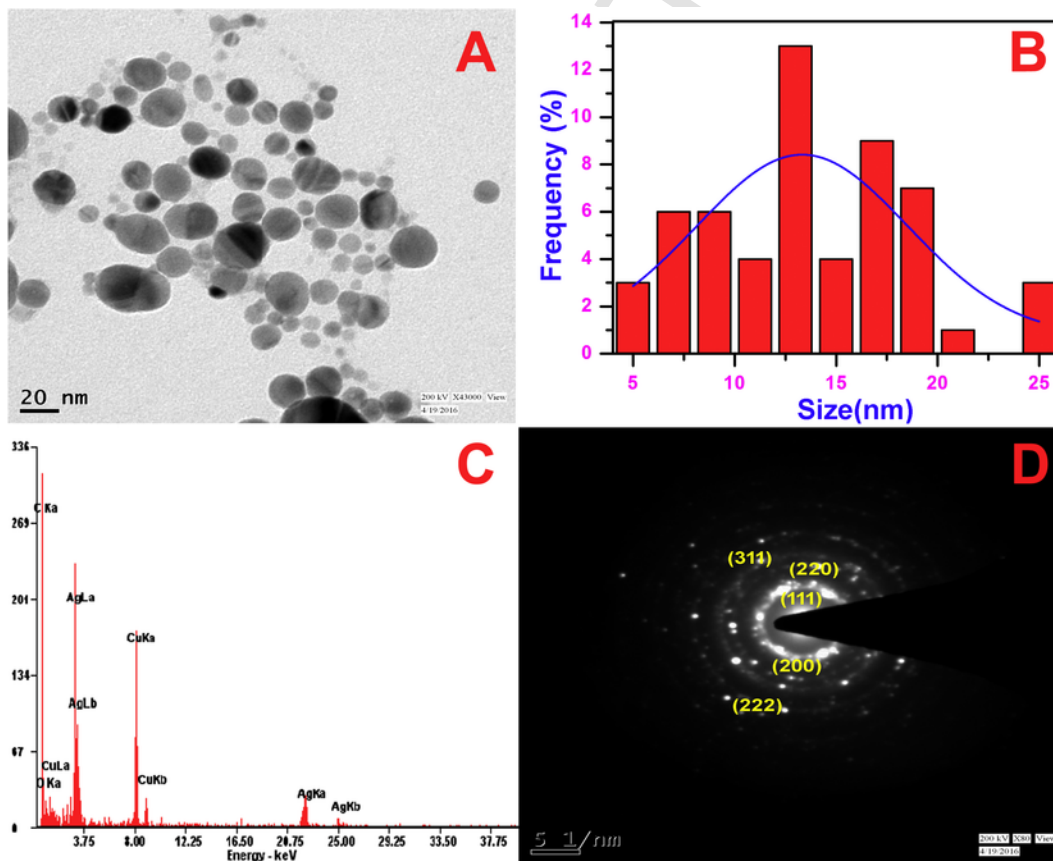


Fig. 1. HR-TEM morphology (A), size histogram plot (B), EDX analysis (C) and SAED pattern (D) of SNPs dispersed in 10% MeOH/H<sub>2</sub>O.

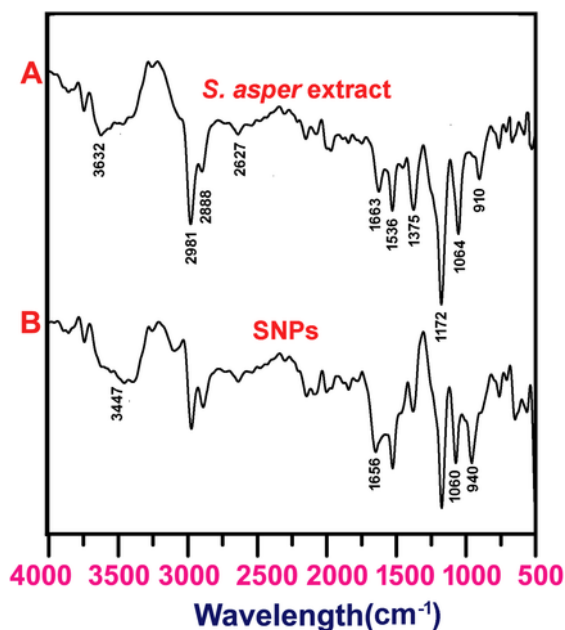


Fig. 2. FT-IR stretching bands of (A) SAE and (B) SNPs.

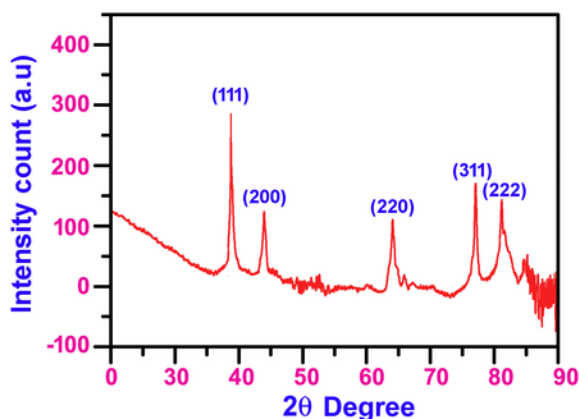


Fig. 3. XRD pattern image to represent the degree of crystallinity of SNPs.

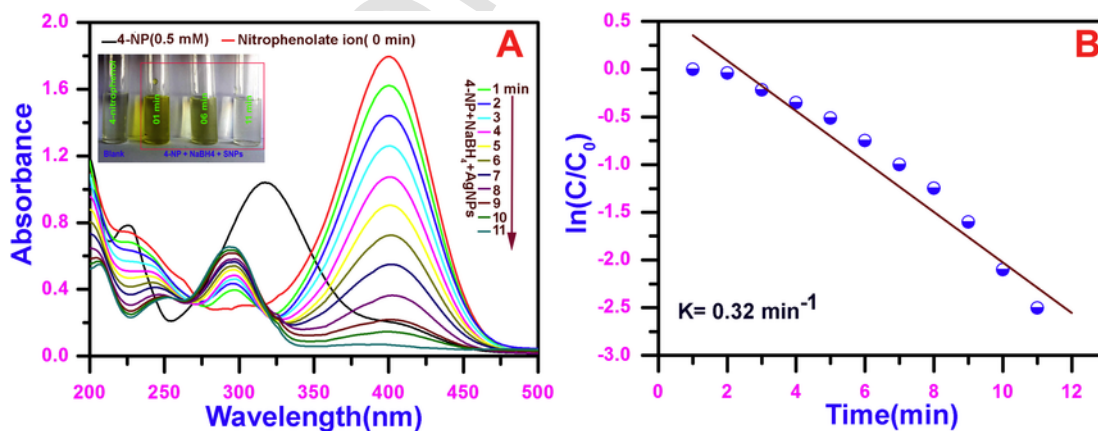


Fig. 4. Time dependent UV-vis spectra for the catalytic degradation of 4-NP by  $\text{NaBH}_4$  in presence of (A) SNPs, (inset: visual image of blank 4-NP and after catalytic degradation at 1, 6 and 11 min) (B) plot of  $\ln(C_0/C)$  versus time plot for 4-NP for rate constant estimation. Conditions:  $[4\text{-NP}] = 0.5 \text{ mM}$ ;  $[\text{SNPs}] = 0.14 \text{ nM}$ ;  $[\text{NaBH}_4] = 0.02 \text{ M}$ . (For interpretation of the references to color in this figure, the reader is referred to the web version of this article.)

efficient (0.9),  $D$  is average crystal size,  $\lambda$  is the X-ray wavelength ( $\lambda = 1.54 \text{ \AA}$ ),  $\beta_{1/2}$  is the full width half maximum intensity (FWHM) in radians and  $\theta$  is Bragg's angle.

### 3.3. Optical energy gap determination

According to Tauc's theory, the optical band-gap energy ( $E_g$ ) of SNPs can be monitored from the absorbance spectra. The calculation of  $E_g$  was done by plotting  $(\alpha h\nu)^2$  vs  $(h\nu)$  according to the Eq. (1):

$$(\alpha h\nu) = C(\alpha h\nu - E_g)^{1/n} \quad (1)$$

Thus  $E_g$  was evaluated by extra plotting the linear part (Fig. S4) of the curve [47]. The significance all terms in Eq. (1) are described as, where  $\alpha$  = the absorption coefficient (calculated from the relation  $A = I/I_0 = e^{-\alpha d}$  or using deduced from Beer-Lambert's relation,  $\alpha = 2.303A/d$ , where  $d$  = path length of the quartz cuvette,  $A$  = absorbance of SNPs) [48],  $h\nu$  = photon energy,  $E_g$  = the direct band gap energy,  $C$  is a constant,  $n = 1/2$  for direct allowed transition for AgNPs [49]. It was revealed that absorption edge of SNPs shows blue shift compared to their bulk counterparts (Fig. S4). This observation clearly confirmed the quantum confinement effect of the AgNPs. However, the estimated optical band gap of AgNPs was 2.45 eV.

### 3.4. Catalytic efficiency of SNPs for reduction of 4-NP

The catalytic performance of biogenic SNPs was substantiated through 4-NP reduction in the presence of  $\text{NaBH}_4$  as a reducing agent. In order to evaluate the catalytic activity of noble metal nanoparticles, this is a very popular model reaction. Interestingly, in spite of thermodynamic feasibility ( $E_{4\text{-NP}/4\text{-AP}}^0 = -0.76 \text{ V}$  and  $E_{\text{H}_3\text{BO}_3/\text{BH}_4}^0 = -1.33 \text{ V}$ ) the reaction (i.e. 4-NP to 4-AP) is a kinetically restricted process and does not occur (even in 2 days) without a catalyst.

Fig. 4A shows absorption maxima of aqueous 4-NP at 317 nm which was red shifted (317 nm to 400 nm) with the addition of  $\text{NaBH}_4$  into the solution of 4-NP.

The colorless 4-NP solution was converted into deep yellow color which was due to the formation of 4-nitrophenolate ion [50]. However, with the addition of SNPs (10  $\mu\text{L}$ ), the catalytic degradation process was started (Fig. 4A) by transferring electrons from  $\text{BH}_4^-$

(donor) to nitro compound (acceptor) and both reactants are adsorbed on the particles. Thus, during this catalytic reduction, the deep yellow color of the nitrophenolate ion solution gradually becomes colorless (insitu of Fig. 4A) due to the mere adsorption of the nitrophenolate ion. The absorption maxima at 400nm regularly decreased with the concomitant development of a new band at 298nm which confirmed the formation of 4-AP [51]. In a cross experiment with the only  $\text{NaBH}_4$ , the decrement of the absorption band for nitrophenolate ion was observed (Fig. S5) rather than the development of new peak at 298 nm (i.e. 4-AP was not produced). This interesting phenomenon also strengthens the fact of SNPs induced catalytic degradation phenomena. Fig. 4A clearly shows two isosbestic points at 265 and 321 nm which convincingly demonstrated the formation of 4-AP as a sole product. However, after the complete reduction absorption band at 400nm no longer exists which indicated catalytic degradation had proceeded successfully.

In this overall process, large excess concentration of  $\text{NaBH}_4$  was used to that of 4-nitrophenol. Hence, the catalytic degradation of 4-NP can be considered as a first order reaction. Fig. 4B displayed a linear correlation plot between  $\ln(C/C_0)$  vs. reduction time, where C and  $C_0$  are the absorbances of 4-NP at time t and at initially time 0, respectively. The first order rate constant (K) obtained from the slope (Fig. 4B) was  $0.32 \text{ min}^{-1}$  with a correlation coefficient 0.923.

### 3.5. Catalytic efficiency of AgNPs for reduction of MB

In presence of air or oxygen, organic contaminants like methylene blue (MB) can be degraded by using irradiated noble metal nanoparticles. The activation of SNPs by irradiating UV-light ( $h\nu$ ) generate electron-hole pairs ( $\text{SNPs} + h\nu \rightarrow \text{h}^+ + \text{e}^-$ ) which are very strong reducing ( $\text{O}_2 + \text{e}^- \rightarrow \text{O}_2^-$ ) and oxidising ( $\text{OH}^- + \text{h}^+ \rightarrow \cdot\text{OH}$ ) agent, respectively. In this degradation process the primary oxidant (i.e. hydroxyl radical) arise from adsorbed  $\text{OH}^-$  or adsorbed  $\text{H}_2\text{O}$ , break the MB into simpler organic molecular fragments leading to the concomitant degradation of the dye and oxygen take part to hinder the re-combination of hole-electron pairs (i.e. the overall process is  $\text{MB} + \cdot\text{OH} \rightarrow \text{products}$ ) [52]. The photocatalytic degradation of the MB in presence of synthesized SNPs was monitored by the decrement of the  $\lambda_{\text{max}}$  value of organic dye (i.e. MB) during the UV light exposure time period.

Fig. 5A represented the photocatalytic degradation of MB in presence of SNPs with respect to irradiation time under UV light. The characteristic absorption intensity of deep blue MB dye in presence

of SNPs ( $\lambda_{\text{max}} = 667 \text{ nm}$ ) remain unchanged at zero time but after 10 min exposure of UV light, the absorption intensity was decreased. It was observed that increase in time at the same interval (i.e. 10 min),  $\lambda_{\text{max}}$  intensity of MB led to progressively decline. Visual inspection of degradation process revealed that the deep blue color of MB dye turns colorless after the completion of degradation process (insitu of Fig. 5A). However, the complete reaction occurred after 110min which confirmed the photocatalytic efficiency of this electron relay system. It should be mentioned that there was no change in absorption intensity of control during UV irradiation. The degradation efficiency (%) of SNPs on MB was calculated by using Eq. (2)

$$\text{Dye degradation (\%)} = \frac{C_0 - C}{C_0} \times 100 \quad (2)$$

where  $C_0$  is the initial concentration of the MB and C is the concentration of the MB after t minutes of exposure to UV irradiation. The degradation rate of SNPs was found nearly 91% after 110min (Fig. 5B). Hence, it can be concluded that biogenic SNPs may act as a promising photocatalyst for reduction of MB under UV light.

### 3.6. Evaluation of antibacterial activity

The antibacterial activity of SNPs was carried out against gram-negative bacteria *E. coli* ATCC 25922. The prepared SNPs possess efficient antibacterial activity on human pathogenic strains *E. coli*. Smaller sizes of silver nanoparticles were associated with electronic effects that were brought about as a result of changes in local electronic structures on the surfaces of the bacterial strains. As a result, DNA loses its replication ability of the bacterium as well as growth. From the Fig. 6 among the various concentrations of nanoparticles, the MIC and  $\text{LD}_{50}$  were 2nM and 1 nM respectively against *E. coli*. This observation concludes that SNPs may be used to cure of bacterial infections in future.

### 3.7. Assessment of bio-reactivity of the AgNPs with human serum albumin (HSA)

#### 3.7.1. UV-visible spectroscopic study

In order to investigate the nanoparticles induced physicochemical conformation evolution of serum protein, the interactions of HSA with SNPs were ascertained by the UV-visible spectroscopic study.

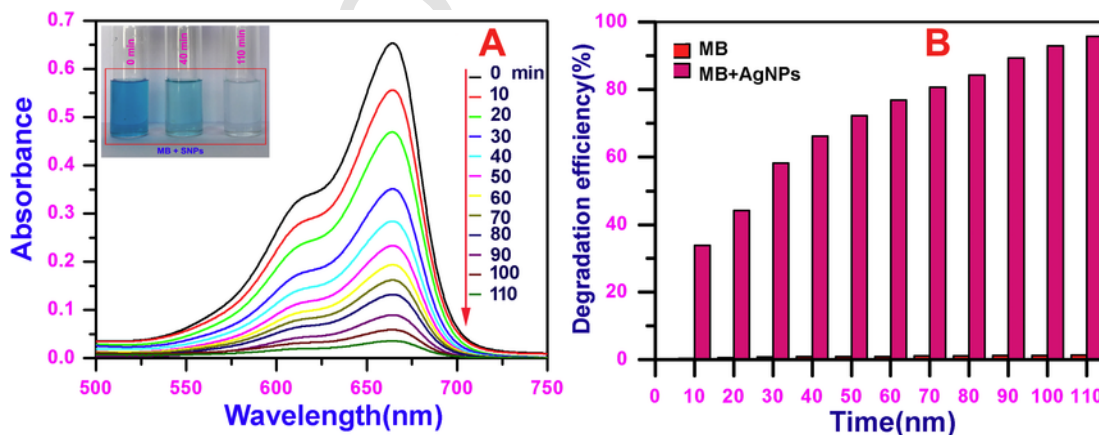


Fig. 5. (A) Estimation of the kinetics of the MB dye degradation by the SNPs at 10 min interval of time. Insitu: visual picture of MB before and after degradation. (B) The efficiency of SNPs on degrading absorption intensity of MB vs time. Condition:  $[\text{MB}] = 5 \mu\text{M}$ ;  $[\text{SNPs}] = 0.14 \text{ nM}$ .

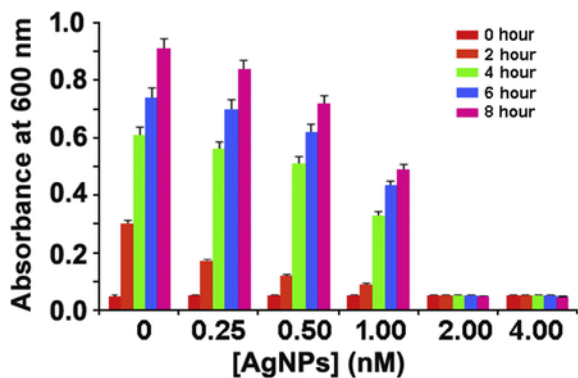


Fig. 6. The effect of various concentrated SNPs against the growth of *E. coli* ATCC 25922 in MH broth at different time intervals.

Fig. 7A revealed that SNPs (5 nM) have strong absorption maxima at 425 nm in absence of HSA which was steadily decreased on increasing concentration of HSA (0 to 5 nM) up to saturation. Interestingly, it should be observed that decrement in absorption maxima due to continuous augmentation of HSA did not result in any peak broadening nor any significant leveled up tail in baseline titration. From these two facts, it should conclude that decrement of absorption spectra of SNPs occur only due to adsorption of HSA on the surface of SNPs

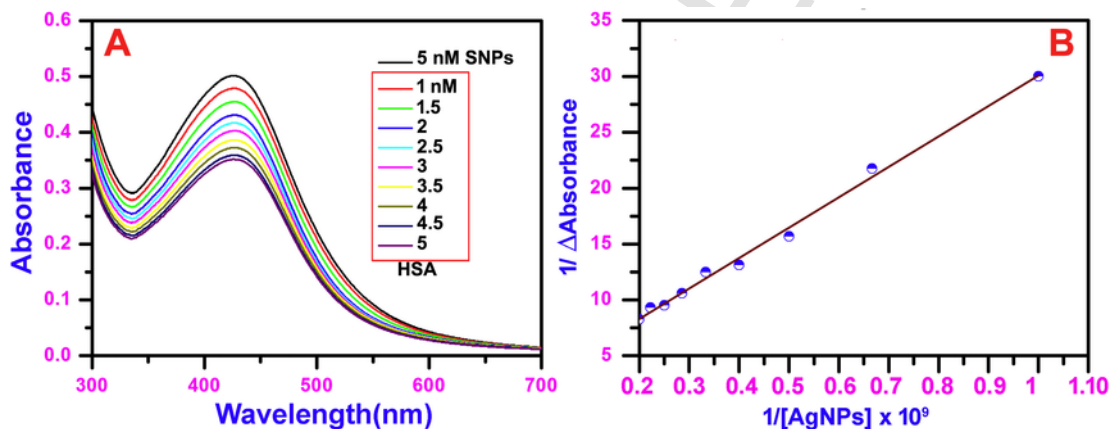


Fig. 7. (A) Absorption spectral changes of SNP (5 nM) after incubation of different concentration of HSA. (B) Benesi-Hildebrand plot for evaluation of binding constant ( $K_{BH} = 1.20 \times 10^8 M^{-1}$ ).

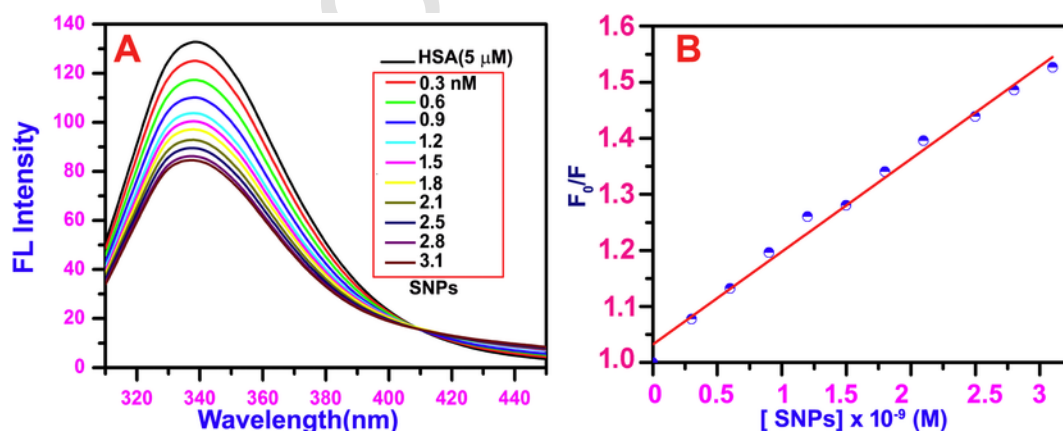


Fig. 8. (A) Emission quenching spectra of HSA ( $5 \mu M$ ) at variable concentrations of SNPs. (B) Stern-Volmer plots for estimation of binding constant ( $K_{SV} = 1.6 \times 10^8 M^{-1}$ ). ( $\lambda_{ex} = 295 \text{ nm}$ , Ex. slit = 5 and Em. slit = 5).

and binding of HSA with SNPs is very prominent rather than aggregation [53]. To investigate the binding affinity of HSA on nanoparticles surface the binding value calculated by using Benesi-Hildebrand Eq. (3),

$$\frac{1}{\Delta A} = \frac{1}{\Delta A_{\max}} + \frac{1}{K_{BH} (\Delta A_{\max})} \times \frac{1}{[M]} \quad (3)$$

where  $\Delta A$  is the difference of absorption spectroscopic maxima between unbound SNPs and bound SNPs upon interaction,  $[M]$  is the concentration of HSA. Fig. 7B represented the linear double reciprocal plot of  $1/[M]$  vs  $1/\Delta A$  and the calculated binding constant ( $K_{BH}$ ) was found  $1.20 \times 10^8 M^{-1}$ . Moreover, the outcome of the absorption studies was convincingly in accordance with previously reported papers where the same type of a non-fluorescent ground-state complex was formed during protein and nanoparticles interaction.

### 3.7.2. Steady-state fluorescence spectroscopic and intrinsic emission quenching studies of HSA by AgNPs

The role of emission spectroscopy on elucidating the high quenching efficiency of intrinsic emission intensity and binding mechanism of serum protein upon interaction with nanoparticles is well established [54]. Fig. 8A represented the impact of SNPs on the intrinsic

emission intensity of HSA upon continuous addition of SNPs. The emission spectrum of HSA mostly comes from one Trp-214 residue (sub-IIA). An intrinsic quenching study for the interaction of HSA with SNPs was done at the Trp-214 site. The fluorescence spectra of native HSA show emission maxima at 340 nm upon excitation at 295 nm. Here, we chose excitation wavelength at 295 nm to neglect the contribution from Tyr residue [55]. From the Fig. 8A it was observed that the intrinsic emission intensity of HSA (5  $\mu$ M) decreased progressively without any shift in emission wavelength on continuous augmentation of different concentration SNPs (0 to 3.1 nM). In the present case, the absence of any shift in intrinsic quenching emission maxima concluded that adsorption of protein on the nanoparticles surface occurs due to close proximity of amino acid residues with nanoparticles surface. Therefore, the quenching in emission intensity of HSA directly attributed to complex formation after interaction with SNPs. In order to resolute correct explanation for reduced emission intensity of protein upon interaction, the minimization of absorption and re-absorption of SNPs at excitation and emission range of HSA is very much important. Thus the correction of inner filter effect was applied according to the following Eq. (4).

$$F_{\text{corr}} = F_{\text{obs}} \times e^{\frac{(A_{\text{exc}} + A_{\text{emi}})}{2}} \quad (4)$$

Where,  $F_{\text{obs}}$  and  $F_{\text{corr}}$  are the observed and corrected emission intensities, respectively.  $A_{\text{exc}}$  and  $A_{\text{emi}}$  are the interacting solution absorption at the excitation and emission wavelengths, respectively. The quenching mechanism was analyzed by Stern-Volmer equation after the correction of inner filter effects according to the following Eq. (5).

$$\frac{F_0}{F} = 1 + K_q \tau_0 [Q] = 1 + K_{\text{SV}} [Q] \quad (5)$$

where  $F_0$  and  $F$  symbolize the utmost intrinsic emission intensities in the absence and presence of AgNPs, respectively.  $K_q$ =apparent bimolecular quenching constant of the biological macromolecule,  $\tau_0$  is the unquenched average lifetime of HSA which is of the order of  $\sim 10^{-8}$  s (5 ns) [56],  $[Q]$ =the molar concentration of quencher (i.e. SNPs), and  $K_{\text{SV}}$ =the Stern-Volmer quenching constant, (which represents the efficiency of the quencher).  $[Q]$ =the concentration of SNPs. Fig. 8B represent Stern-Volmer linear plot and the calculated binding value was found  $1.6 \times 10^8 \text{ M}^{-1}$ . The outcome of the nanoparticles-HSA interaction study was found to be in good agreement with previously reported papers where 5–100 nm size nanoparticles show  $10^8$ – $10^{11} \text{ M}^{-1}$  order  $K_{\text{SV}}$  values [57]. The value of  $K_q$  can be deduced according to the following Eq. (6).

$$K_q = \frac{K_{\text{SV}}}{\tau_0} \quad (6)$$

The obtained  $K_q$  value from protein quenching procedure was  $1.6 \times 10^{16} \text{ M}^{-1}$  and this value was higher than  $K_q$  value of the biopolymer ( $2.0 \times 10^{10} \text{ M}^{-1} \cdot \text{s}^{-1}$ ). Therefore it should be concluded that the intrinsic quenching of lone Trp residue was initiated by HSA through static mechanism rather than dynamic collision.

Meanwhile, In the case of HSA-nanoparticles interaction binding process involved multiple cooperativities in nature because interaction concerned manifold associative interfaces when approaches to nanoparticles surface. Thereby, the assembly of non-fluorescent

HSA-SNPs complex conjugate formation was further delineated according to the double log plot Eq. (7) [57].

$$\log \left[ \frac{F_0 - F}{F} \right] = \log K_b + n \log [Q] \quad (7)$$

The significance of  $F_0$  and  $F$  are same as above described equation,  $K_b$ =binding constant and  $n$ =hill coefficient. In protein-nanoparticle binding studies,  $n$  determined the degree of cooperativity towards nanoparticles surface [57].

Fig. 9 represents the double logarithmic plot of HSA-SNPs system and the evaluated binding ( $K_b$ ) constant was  $1.25 \times 10^8 \text{ M}^{-1}$  obtained from the intercept of the slope. In the present case the hill coefficient ( $n$ ) was found greater than 1 ( $n=1.1$ ) which believably appreciated the existence of cooperative binding (i.e. after adsorption of single HSA protein molecule on to SNPs surface, the affinity of other HSA molecule significantly increased towards SNPs surface in a superlinear way) nature upon interaction of HSA-SNPs system [57]. Thus the  $K_b$  value compellingly confirmed the subsistence of a prominent interaction between HSA and SNPs (comparable binding value obtained from absorbance study) which supported by other reports [38,58].

In order to estimate the feasibility of interaction, free energy of the HSA-SNPs system was calculated according to the Eq. (8) [58].

$$\Delta G = -RT \ln K_b \quad (8)$$

where  $R$ =the universal gas constant,  $T$ =room temperature, and  $K_b$ =the binding constant value obtained from the double logarithmic plot. The calculated free energy value for our system was found  $-46.16 \text{ kJ mol}^{-1}$ . The negative  $\Delta G$  value clearly indicated that the overall process is thermodynamically favorable [58].

### 3.7.3. Measurement of constant wavelength synchronous fluorescence spectra (CWSFS)

Synchronous Fluorescence spectroscopy has been used as an additional evidence of ground state complex formation after interaction of HSA with SNPs and very much important to evaluate the molecular environment in the environs of Tyr and Trp residues.

Wherein, Constant Wavelength Synchronous Fluorescence Spectra (CWSFS) were obtained by synchronously scanning emission and

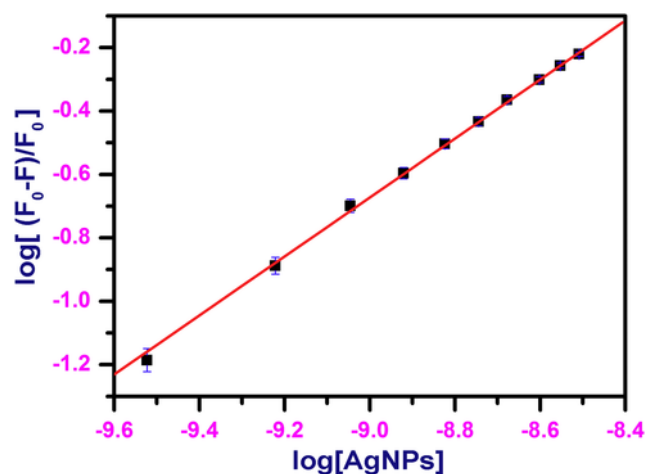


Fig. 9. Evaluation of binding constant for HSA-SNPs by the double logarithmic plot.

excitation monochromators of HSA at different scanning interval  $\Delta\lambda$  ( $\Delta\lambda = \lambda_{\text{emission}} - \lambda_{\text{excitation}}$ ). The characteristic information for Tyr and Trp residue were obtained at  $\Delta\lambda = 15$  nm and 60 nm respectively [59]. Fig. 10 shows that the CWSFS of HSA-SNPs gradually decreased with continued augmentation of SNPs and any shift in emission maxima was absent. These results evidenced that during the course of interaction a noteworthy quenching in emission maxima of protein happened with the production of nonfluorescent ground state HSA-SNPs complex without any considerable perturbation in the microenvironment or polarity around the local area of Tyr and Trp amino acid residues of HSA [38].

### 3.7.4. Time-resolved fluorescence spectroscopic measurement

In HSA protein only single Trp residue is located in the biologically imperative subdomain IIA ligand binding site at amino acid position 214. Therefore the fluorescence lifetime measurement by using Trp as an intrinsic probe for monitoring structural evaluation upon interaction with nanoparticles is potentially very much important. Thus, In order to validate ground state complex formation via a static quenching mechanism excited state lifetime measurements of HSA (10  $\mu\text{M}$ ) were performed before and after augmentation of Ag-NPs. The experimental results of time-resolved fluorescence decay profiles,  $R(t)$  were estimated by inbuilt Horiba EZ time software unit according to the following expression Eq. (9) [60].

$$R(t) = \sum_{i=1}^n \alpha_i \exp\left(-\frac{t}{\tau_i}\right) \quad (9)$$

Here,  $n$  = number of distinct decay components and  $\tau_i$  and  $\alpha_i$  are excited-state fluorescence lifetimes and the pre-exponential factors related to the  $i$ th component, respectively [60]. Fig. 11 displayed fluorescence decays profile of tryptophan in pure HSA protein (observed at 340 nm, CP buffer at pH=7.05) and in HSA-conjugated SNPs (3 nM). The intrinsic fluorescence intensity decay profiles are adequately best fitted to a sum of three exponentials function (Fig. 11) with average lifetime values of 5.13 ns (pure HSA) and 5.15 ns (for HSA-SNPs conjugate). For pure HSA three lifetime components and pre-exponential factors are listed in Table 1 which is in good agreement with current reports [61]. The average lifetime values of HSA upon the assimilation of SNPs clearly revealed the absence of notable reduction in lifetime compared to pure HSA which is im-

posed on the formation of nonfluorescent HSA-SNPs ground-state complex. It has been well characterizing that the decay time of unbound fluorophore did not degassed upon formation of static ground state complexes because time-resolved spectroscopic analysis only deliberates the lifetime of the free fluorophore. Indeed, dynamic quenching (actually a rate process) act on the whole excited state population and accordingly decreases with the mean decay time of the complete excited-state population [61]. Thus relying on the result of time-resolved fluorescence spectroscopy it was conjectured that quenching in fluorescence spectra of HSA upon addition of SNPs appeared via a static quenching mechanism process. The results are convincingly in good conformity with the upshot of the steady-state fluorescence quenching experiment.

### 3.7.5. Excitation–emission matrix spectroscopic analysis

In order to make the protein-nanoparticle interaction more scientific 3D emission spectroscopy (or excitation–emission matrix spectroscopy) has now become a trustworthy technique in disentanglement the study of binding-induced conformational changes in proteins. The excellent advantage of the method is that it delineates the characteristic emission of the intrinsic fluorophore by concurrently varying the excitation and emission wavelengths. Fig. 12A and B represent the contour map and 3D fluorescence spectra of blank HSA and HSA-SNPs (Fig. 12C and D) complex where peak a and peak b represent the Rayleigh scattering peak ( $\lambda_{\text{ex}} = \lambda_{\text{em}}$ ) and second-order scattering respectively. The appearance of such peaks (i.e. peak a and b) attributed to the  $\pi$ - $\pi^*$  transition of the distinct polypeptide backbone structure C=O of HSA [62]. It is noticeable that 3D fluorescence spectra of HSA exhibit another two peaks where peak 1 represent Rayleigh scattering peak 1 ( $\lambda_{\text{em}} = \lambda_{\text{ex}}$ ) and peak 2 directly demonstrate the spectral behavior and micro-environmental polarity around Tyr and Trp residues [63]. 3D fluorescence spectra of HSA-SNPs system exhibited fluorescence quenching of peak 1 and 2 without any alteration in Stokes shift i.e. during the interaction of HSA with SNPs the environment in the vicinity of Tyr and Trp residue did not undergo any considerable modification (results are shown in Table S1). The negligible effect of SNPs on the core structure of HSA upon interaction was also evidenced by CWSFS study.

### 3.8. Circular dichroism and conformational analysis

Circular dichroism (CD) spectroscopy has been popularly used to assess the conformational evaluation of proteins after the interaction.

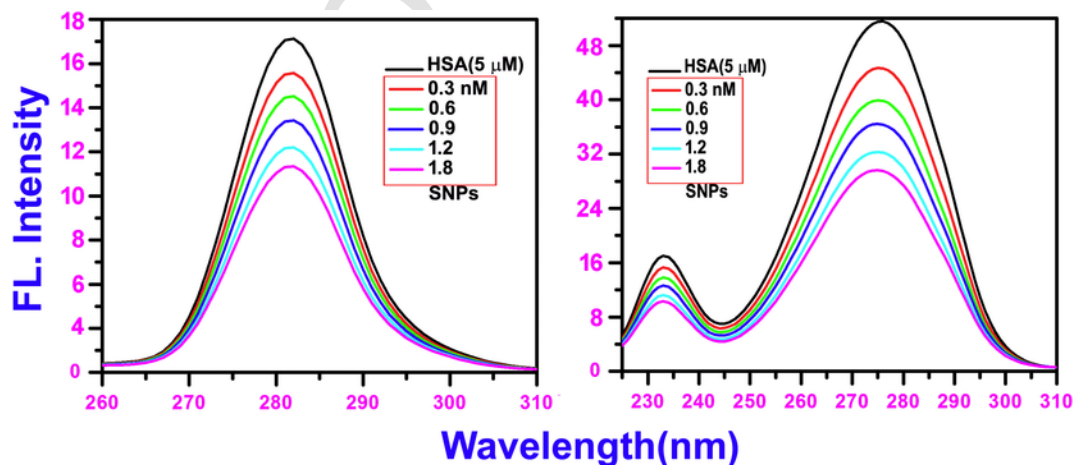


Fig. 10. Synchronous emission spectra of HSA-SNPs system with various concentrations of SNPs (A)  $\Delta\lambda = 15$  nm and (B)  $\Delta\lambda = 60$  nm.

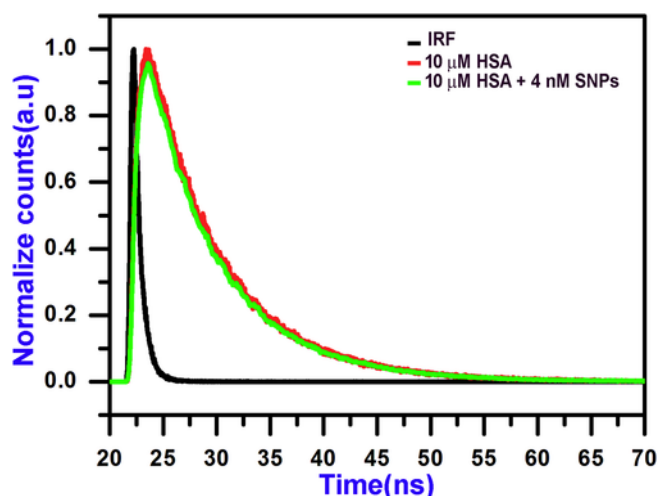


Fig. 11. Time-resolved fluorescence intensity decay profile of blank (red line) HSA (10  $\mu\text{M}$ ) and (green line) HSA-SNPs system ( $\lambda_{\text{em}} = 340 \text{ nm}$ , [SNPs] = 4 nM). Black line represents Instrument Resonance Function (IRF). (For interpretation of the references to color in this figure legend, the reader is referred to the web version of this article.)

Table 1

Time-resolved photoluminescence decay parameters of HSA and HSA-SNPs ( $\lambda_{\text{emission}} = 340 \text{ nm}$ ).

System	$\alpha_1$	$\tau_1$ (ns)	$\alpha_2$	$\tau_2$ (ns)	$\alpha_3$	$\tau_3$ (ns)	$\langle \tau \rangle^a$ (ns)	$\chi^2$
HSA (10 $\mu\text{M}$ )	0.18	0.22	0.31	4.11	0.49	7.82	5.14	1.06
HSA-SNPs	0.26	0.32	0.20	3.90	0.57	7.57	5.17	1.13

$\langle \tau \rangle = \tau_1 \alpha_1 + \tau_2 \alpha_2 + \tau_3 \alpha_3$  and the magnitude of  $\chi^2$  indicate best fitting. <sup>a</sup>  $\pm 2\%$ .

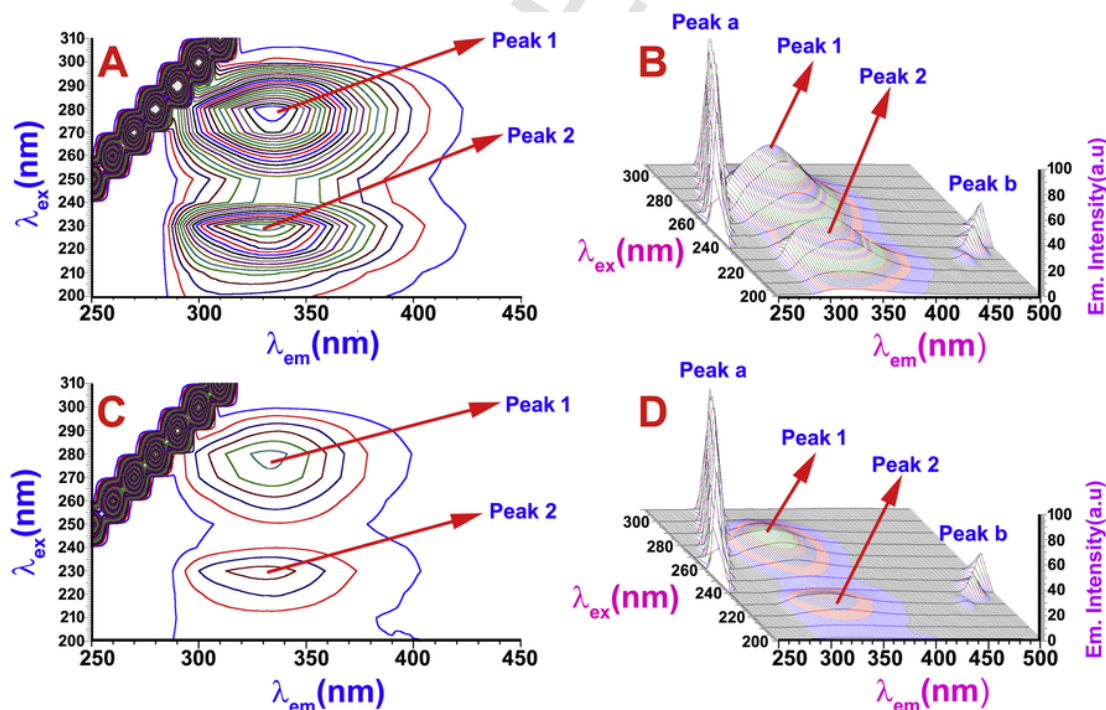


Fig. 12. 3D matrix contour diagram and bird view emission spectra of HSA 5  $\mu\text{M}$  (A, B) and HSA-SNPs binary complex (C, D). [SNPs] = 4 nM.

In proteins, the peptide structure of polypeptide backbones is mostly dominated by the  $\pi^*-\pi^*$  and  $n-\pi^*$  transitions of amide groups in the far ultraviolet region [64]. In Fig. 13 two negative bands (at 208 nm and 222 nm) clearly indicated in the CD spectra of HSA (blank, 1  $\mu\text{M}$ ) and after the continued addition of SNPs, the negative bands were gradually degassed without changing the shape and peak position of CD spectra. The continued decrement in the intensity of CD spectra was originated as a result of decrease in  $\alpha$ -helix content with a minimal unfolding of main peptide strand upon interaction of SNPs with amino acid residues present in HSA. The percentage of  $\alpha$ -helix,  $\beta$ -sheet and random coil content of HSA was calculated by using in-built JASCO CD software unit are shown in Table 2. The results show that  $\alpha$ -helical content of native HSA (56.2%) decreased (52.9%) upon interaction with SNPs at a final saturation concentration of 2  $\mu\text{M}$ . Interestingly, it was observed that during the association of HSA with SNPs the shape and peak position of CD spectra remain unchanged which convincingly confirmed the presence of unaltered structure of HSA after binding with SNPs. Thus, it can be concluded that interaction of SNPs did not hamper the stability of peptide backbone of HSA [45].

### 3.9. Zeta ( $\zeta$ ) potential assay of HSA-AgNPs conjugates

To investigate the variation in net surface charge of HSA upon interaction with SNPs the assessment of zeta potential has been carried out. It is familiar that measurement of the zeta potential is directly associated with the electrical potential property at the surface of SNPs and potential the depth of the double layer [65]. The aqueous dispersion of SNPs and crude extract of *S. asper* leaf exhibited zeta potential value of  $-25.3$  and  $-17.6 \text{ mV}$  (Fig. S6), respectively. Large negative zeta potential value ascribed the formation of stable dispersion of nanoparticles. Thus on describing HSA-SNPs interaction, zeta potential study gives the efficacy of binding as this will change the overall surface charge. In neutral solution, HSA protein had a net negative

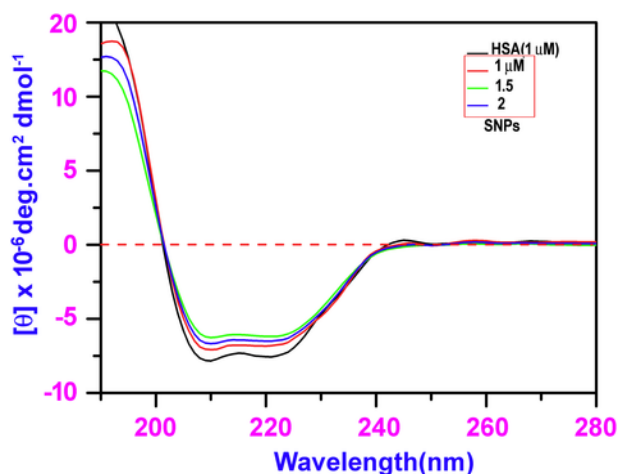


Fig. 13. Intrinsic circular dichroic spectral changes of HSA (1  $\mu\text{M}$ ) at 0–2  $\mu\text{M}$  SNPs concentration.

Table 2

Estimation of  $\alpha$ -helix,  $\beta$ -sheet and random coil in HSA in presence of different concentrations of SNPs (pH = 7.05, 25  $^{\circ}\text{C}$ ).

System	SNPs/proteins	% $\alpha$ -helix	% $\beta$ -sheet	% random coil
HSA	0	56.2	25.9	17.9
	1	54.5	26.7	18.8
	1.5	53.1	27.4	19.5
	2.0	51.1	28.8	20.1

charge ( $-9$ ,  $-8$  and  $-12$  for domains I, II and III, respectively) [37] and exhibit zeta potential value of  $-15.5$  mV. After assimilation of SNPs into HSA, the zeta potential value (Fig. S6) of HSA-SNPs ( $-49.4$  mV) system tends to more negative in compared to SNPs ( $-25.3$  mV). The observed zeta potential value indicated that interparticle aggregation was minimized due to the increment of electrostatic charge at HSA-SNPs surface in compared to blank SNPs. Owing to the above-mentioned shortfall it can be explained that protein molecules effectively adsorbed on to the external surfaces of SNPs and stabilized the HSA-SNPs bioconjugates.

#### 4. Conclusion

In summary, this work successfully coalesces the green chemistry and nanotechnology by a single SNPs formation from an eco-friendly renewable plant leaf source. This study may be a worthwhile addition for healthy nanotechnological development. The morphological property and synthesis were well estimated by UV-visible, FT-IR, DLS, zeta potential, FE-SEM, HR-TEM, EDX, and XRD technique. Multiple applicative studies upon SNPs explored the remarkable catalytic degradation efficiency on 4-NP to 4-AP and MB dye within a diminutive irradiation time. Thus SNPs mediated degradation offered an alternative cost-saving eco-friendly method rather than the use of metallic reagents. The SNPs also exhibited potential of strong antibacterial activity against *E. coli* ATCC 25922. Importantly, in interaction study SNPs shows a strong affinity towards HSA and the investigation was fruitfully convinced by multiple spectroscopic methods. It is shown that interaction of SNPs with HSA resolute the formation of HSA-SNPs conjugate. The results inferred that the course of binding was completely static and proceed with good spontaneity. However, on the basis of studied applicative advancements of the whole study and according to the overall accumulated knowledge, we strongly demand that this smart biogenic SNPs can be used as bacte-

ricidal in wound healing, water purification which will revolutionize the field of medicine due to it significantly effortless application. With these systematic and comprehensive study, we anticipated that in the near future our study could be performed a significantly meaningful role for the secure application of Nanoparticles in biological systems and industrial purpose as well.

#### Acknowledgements

This work was financially supported by the Department of Science and Technology (DST) Science and Engineering Research Board (SERB), Govt. of India, No SB/FT/CS-051/2013 (SERB/F/3694/2015-2016). Somnath Das gratefully acknowledges the University Grants Commission (UGC) (award letter number: 2061610244/19-06-2016), Govt. of India, New Delhi for the award of Junior Research Fellowship (JRF). Departmental instrumental facilities from DST-FIST and UGC-SAP programs are gratefully acknowledged. We gratefully acknowledge the help provided by USIC, Vidyasagar University for doing spectroscopic measurements.

#### Appendix A. Supplementary data

Supplementary data to this article can be found online at <https://doi.org/10.1016/j.molliq.2018.02.111>.

#### References

- [1] V.K. Gupta, M.L. Yola, N. Atar, Z. Üstündağ, A.O. Solak, Electrochemical studies on graphene oxide-supported metallic and bimetallic nanoparticles for fuel cell applications, *J. Mol. Liq.* 191 (2014) 172–176.
- [2] M.L. Yola, T. Eren, N. Atar, H. Saral, I. Ermis, Direct-methanol fuel cell based on functionalized graphene oxide with mono-metallic and bi-metallic nanoparticles: electrochemical performances of nanomaterials for methanol oxidation, *Electroanalysis* 28 (2016) 570–579.
- [3] J. Panyam, V. Labhasetwar, Biodegradable nanoparticles for drug and gene delivery to cells and tissue, *Adv. Drug Deliv. Rev.* 55 (2003) 329–347.
- [4] X. Michalet, F.F. Pinaud, L.A. Bentolila, J.M. Tsay, S. Doose, J.J. Li, G. Sundaresan, A.M. Wu, S.S. Gambhir, S. Weiss, Quantum dots for live cells, in vivo imaging, and diagnostics, *Science* 307 (2005) 538–544.
- [5] X. Huang, L. Li, H. Qian, C. Dong, J. Ren, A resonance energy transfer between chemiluminescent donors and luminescent quantum-dots as acceptors (CRET), *Angew. Chem. Int. Ed.* 45 (2006) 5140–5143.
- [6] A.R. Clapp, I.L. Medintz, B.R. Fisher, G.P. Anderson, H. Mattoussi, Can luminescent quantum dots be efficient energy acceptors with organic dye donors?, *J. Am. Chem. Soc.* 127 (2005) 1242–1250.
- [7] M. De, P.S. Ghosh, V.M. Rotello, Applications of nanoparticles in biology, *Adv. Mater.* 20 (2008) 4225–4241.
- [8] K. Kathiresan, S. Manivannan, M.A. Nabeel, B. Dhivya, Studies on silver nanoparticles synthesized by a marine fungus, *Penicillium fellutanum* isolated from coastal mangrove sediment, *Colloids Surf. B: Biointerfaces* 71 (2009) 133–137.
- [9] V. Sridhara, K. Pratima, G. Krishnamurthy, B. Sreekanth, Vegetable assisted synthesis of silver nanoparticles and its antibacterial activity against two human pathogens, *Asian J. Pharm. Clin. Res.* 6 (2013) 53–57.
- [10] S. Das, M.N. Aktara, N.K. Sahoo, P.K. Jha, M. Hossain, Sensitive and robust colorimetric assay of  $\text{Hg}^{2+}$  and  $\text{S}^{2-}$  in aqueous solution directed by 5-sulfosalicylic acid-stabilized silver nanoparticles for wide range application in real samples, *J. Environ. Chem. Eng.* 5 (2017) 5645–5654.
- [11] M. Beytur, F. Kardeş, O. Akyıldırım, A. Özkan, B. Bankoğlu, H. Yüksek, M.L. Yola, N. Atar, A highly selective and sensitive voltammetric sensor with molecularly imprinted polymer based silver@gold nanoparticles/ionic liquid modified glassy carbon electrode for determination of ceftizoxime, *J. Mol. Liq.* 251 (2018) 212–217.
- [12] N. Atar, T. Eren, M. Yola, H. Gerengi, S. Wang, Fe@Ag nanoparticles decorated reduced graphene oxide as ultrahigh capacity anode material for lithium-ion battery, *Ionics* 21 (2015) 3185–3192.
- [13] M.L. Yola, T. Eren, N. Atar, S. Wang, Adsorptive and photocatalytic removal of reactive dyes by silver nanoparticle-colemanite ore waste, *Chem. Eng. J.* 242 (2014) 333–340.
- [14] N. Atar, T. Eren, B. Demirdögen, M.L. Yola, M.O. Çağlayan, Silver, gold, and silver@gold nanoparticle-anchored L-cysteine-functionalized reduced graphene oxide as electrocatalyst for methanol oxidation, *Ionics* 21 (2015) 2285–2293.

- [15] L.M. Liz-Marzán, I. Lado-Touriño, Reduction and stabilization of silver nanoparticles in ethanol by nonionic surfactants, *Langmuir* 12 (1996) 3585–3589.
- [16] M.P. Pileni, Fabrication and physical properties of self-organized silver nanocrystals, In: *Pure and Applied Chemistry*, 2000, p. 53.
- [17] Y.-P. Sun, P. Atornigijawat, M.J. Meziani, Preparation of silver nanoparticles via rapid expansion of water in carbon dioxide microemulsion into reductant solution, *Langmuir* 17 (2001) 5707–5710.
- [18] M.R. Bindhu, M. Umadevi, Antibacterial and catalytic activities of green synthesized silver nanoparticles, *Spectrochim. Acta A Mol. Biomol. Spectrosc.* 135 (2015) 373–378.
- [19] L.S. Devi, S.R. Joshi, Ultrastructures of silver nanoparticles biosynthesized using endophytic fungi, *J. Microsc. Ultrastruct.* 3 (2015) 29–37.
- [20] M.J. Ahmed, G. Murtaza, A. Mehmood, T.M. Bhatti, Green synthesis of silver nanoparticles using leaves extract of *Skimmia laureola*: characterization and antibacterial activity, *Mater. Lett.* 153 (2015) 10–13.
- [21] S.A. Wadhvani, U.U. Shedbalkar, R. Singh, M.S. Karve, B.A. Chopade, Novel polyhedral gold nanoparticles: green synthesis, optimization and characterization by environmental isolate of *Acinetobacter* sp. SW30, *World J. Microbiol. Biotechnol.* 30 (2014) 2723–2731.
- [22] J. Annamalai, T. Nallamuthu, Green synthesis of silver nanoparticles: characterization and determination of antibacterial potency, *Appl. Nanosci.* 6 (2016) 259–265.
- [23] P. Velmurugan, K. Anbalagan, M. Manosathyadevan, Green synthesis of silver and gold nanoparticles using *Zingiber officinale* root extract and antibacterial activity of silver nanoparticles against food pathogens, *Bioprocess Biosyst. Eng.* 37 (2014) 1935–1943.
- [24] B. Ahmad, S. Parveen, R.H. Khan, Effect of albumin conformation on the binding of ciprofloxacin to human serum albumin: a novel approach directly assigning binding site, *Biomacromolecules* 7 (2006) 1350–1356.
- [25] S. Ahmed, M. Ahmad, B.L. Swami, S. Ikram, A review on plants extract mediated synthesis of silver nanoparticles for antimicrobial applications: a green expertise, *J. Adv. Res.* 7 (2016) 17–28.
- [26] N. Durán, P.D. Marcato, G.I.H. De Souza, O.L. Alves, E. Esposito, Antibacterial effect of silver nanoparticles produced by fungal process on textile fabrics and their effluent treatment, *J. Biomed. Nanotechnol.* 3 (2007) 203–208.
- [27] Z. Aghili, S. Taheri, H.A. Zeinabad, L. Pishkar, A.A. Saboury, A. Rahimi, M. Falahati, Investigating the interaction of Fe nanoparticles with lysozyme by biophysical and molecular docking studies, *PLoS ONE* 11 (2016) 1–21.
- [28] P. Esfandfar, M. Falahati, A. Saboury, Spectroscopic studies of interaction between CuO nanoparticles and bovine serum albumin, *J. Biomol. Struct. Dyn.* 34 (2016) 1962–1968.
- [29] L. Pishkar, S. Taheri, S. Makarem, H. Alizadeh Zeinabad, A. Rahimi, A.A. Saboury, M. Falahati, Studies on the interaction between nanodiamond and human hemoglobin by surface tension measurement and spectroscopy methods, *J. Biomol. Struct. Dyn.* 35 (2017) 603–615.
- [30] H.A. Zeinabad, E. Kachoei, A.A. Saboury, I. Kostova, F. Attar, M. Vaezzadeh, M. Falahati, Thermodynamic and conformational changes of protein toward interaction with nanoparticles: a spectroscopic overview, *RSC Adv.* 6 (2016) 105903–105919.
- [31] P. Kumar, M. Govindaraju, S. Senthamselvi, K. Premkumar, Photocatalytic degradation of methyl orange dye using silver (Ag) nanoparticles synthesized from *Ulva lactuca*, *Colloids Surf. B: Biointerfaces* 103 (2013) 658–661.
- [32] L. Szpyrkowicz, Hydrodynamic effects on the performance of electro-coagulation/electro-floitation for the removal of dyes from textile wastewater, *Ind. Eng. Chem. Res.* 44 (2005) 7844–7853.
- [33] Y.H. Kim, R. Hensley, Effective control of chlorination and dechlorination at wastewater treatment plants using redox potential, *Water Environ. Res.* 69 (1997) 1008–1014.
- [34] V. Gómez, M.S. Larrechi, M.P. Callao, Kinetic and adsorption study of acid dye removal using activated carbon, *Chemosphere* 69 (2007) 1151–1158.
- [35] S.K. Kansal, M. Singh, D. Sud, Studies on TiO<sub>2</sub>/ZnO photocatalysed degradation of lignin, *J. Hazard. Mater.* 153 (2008) 412–417.
- [36] V. Jafari Azad, S. Kasravi, H. Alizadeh Zeinabad, M. Memar Bashi Aval, A.A. Saboury, A. Rahimi, M. Falahati, Probing the conformational changes and peroxidase-like activity of cytochrome c upon interaction with iron nanoparticles, *J. Biomol. Struct. Dyn.* 35 (2017) 2565–2577.
- [37] S. Ambika, M. Sundarajan, Green biosynthesis of ZnO nanoparticles using *Vitex negundo* L. extract: spectroscopic investigation of interaction between ZnO nanoparticles and human serum albumin, *J. Photochem. Photobiol. B Biol.* 149 (2015) 143–148.
- [38] M. Beg, A. Maji, A.K. Mandal, S. Das, M.N. Aktara, P.K. Jha, M. Hossain, Green synthesis of silver nanoparticles using *Pongamia pinnata* seed: characterization, antibacterial property, and spectroscopic investigation of interaction with human serum albumin, *J. Mol. Recognit.* 30 (2017), (e2565-n/a).
- [39] M. Beg, A. Maji, A.K. Mandal, S. Das, P.K. Jha, M. Hossain, Spectroscopic investigation on interaction of biogenic, *Croton bonplandianum* leaves extract mediated potential bactericidal silver nanoparticles with human hemoglobin and human serum albumin, *J. Biomol. Struct. Dyn.* (2017) 1–13.
- [40] A. Maji, M. Beg, A.K. Mandal, S. Das, P.K. Jha, M. Hossain, Study of the interaction of human serum albumin with *Alstonia scholaris* leaf extract-mediated silver nanoparticles having bactericidal property, *Process Biochem.* 60 (2017) 59–66.
- [41] P.V. Sharma, Dravyagun Vigyan, In: *Dravyagun Vigyan*, 2013, pp. 233–344.
- [42] R.P. Rastogi, B.N. Dhawan, Anticancer and antiviral activities in indian medicinal plants: a review, *Drug Dev. Res.* 19 (1990) 1–12.
- [43] S. Rastogi, D.K. Kulshreshtha, A.K.S. Rawat, *Streblus asper* Lour. (Shakhotaka): a review of its chemical, pharmacological and ethnomedicinal properties, *Evid. Based Complement. Alternat. Med.* 3 (2006) 217–222.
- [44] J.R.G. Navarro, M.H.V. Werts, Resonant light scattering spectroscopy of gold, silver and gold-silver alloy nanoparticles and optical detection in microfluidic channels, *Analyst* 138 (2013) 583–592.
- [45] J.M. Andrews, Determination of minimum inhibitory concentrations, *J. Antimicrob. Chemother.* 48 (2001) 5–16.
- [46] V. Verma, A.C. Tripathi, S.K. Saraf, Bioactive non-sterol triterpenoid from *Streblus asper*: microwave-assisted extraction, HPTLC profiling, computational studies and neuro-pharmacological evaluation in BALB/c mice, *Pharm. Biol.* 54 (2016) 2454–2464.
- [47] B.A. Simmons, S. Li, V.T. John, G.L. McPherson, A. Bose, W. Zhou, J. He, Morphology of CdS nanocrystals synthesized in a mixed surfactant system, *Nano Lett.* 2 (2002) 263–268.
- [48] R. Seoudi, A. Shabaka, W.H. Eisa, B. Anies, N.M. Farage, Effect of the prepared temperature on the size of CdS and ZnS nanoparticle, *Phys. B Condens. Matter* 405 (2010) 919–924.
- [49] R. Zamiri, H. Abbastabar Ahangar, A. Zakaria, G. Zamiri, M. Shabani, B. Singh, J.M.F. Ferreira, The structural and optical constants of Ag(2)S semiconductor nanostructure in the far-infrared, *Chem. Cent. J.* 9 (2015) 28.
- [50] S. Saha, A. Pal, S. Kundu, S. Basu, T. Pal, Photochemical green synthesis of calcium-alginate-stabilized ag and au nanoparticles and their catalytic application to 4-nitrophenol reduction, *Langmuir* 26 (2010) 2885–2893.
- [51] K.B. Narayanan, N. Sakthivel, Heterogeneous catalytic reduction of anthropogenic pollutant, 4-nitrophenol by silver-bionanocomposite using *Cylindrocodium floridanum*, *Bioresour. Technol.* 102 (2011) 10737–10740.
- [52] J. Zhao, X. Yang, Photocatalytic oxidation for indoor air purification: a literature review, *Build. Environ.* 38 (2003) 645–654.
- [53] S.P. Boulos, T.A. Davis, J.A. Yang, S.E. Lohse, A.M. Alkilany, L.A. Holland, C.J. Murphy, Nanoparticle–protein interactions: a thermodynamic and kinetic study of the adsorption of bovine serum albumin to gold nanoparticle surfaces, *Langmuir* 29 (2013) 14984–14996.
- [54] F. Cañaveras, R. Madueño, J.M. Sevilla, M. Blázquez, T. Pineda, Role of the functionalization of the gold nanoparticle surface on the formation of bioconjugates with human serum albumin, *J. Phys. Chem. C* 116 (2012) 10430–10437.
- [55] B. Hicks, M. White, C.A. Ghiron, R.R. Kuntz, W.A. Volkert, Flash photolysis of human serum albumin: characterization of the indole triplet absorption spectrum and decay at ambient temperature, *Proc. Natl. Acad. Sci. U. S. A.* 75 (1978) 1172–1175.
- [56] J.R. Lakowicz, G. Freshwater, G. Weber, Nanosecond segmental mobilities of tryptophan residues in proteins observed by lifetime-resolved fluorescence anisotropies, *Biophys. J.* 32 (1980) 591–601.
- [57] S.H.D.P. Lacerda, J.J. Park, C. Meuse, D. Pristiniski, M.L. Becker, A. Karim, J.F. Douglas, Interaction of gold nanoparticles with common human blood proteins, *ACS Nano* 4 (2010) 365–379.
- [58] A. Selva Sharma, M. Ilanchelian, Comprehensive multispectroscopic analysis on the interaction and corona formation of human serum albumin with gold/silver alloy nanoparticles, *J. Phys. Chem. B* 119 (2015) 9461–9476.
- [59] J.N. Miller, Recent developments in fluorescence and chemiluminescence analysis. Plenary lecture, *Analyst* 109 (1984) 191–198.
- [60] J.R. Lakowicz, *Principles of Fluorescence Spectroscopy*, 2009.
- [61] T. Sen, S. Mandal, S. Haldar, K. Chattopadhyay, A. Patra, Interaction of gold nanoparticle with human serum albumin (HSA) protein using surface energy transfer, *J. Phys. Chem. C* 115 (2011) 24037–24044.
- [62] Y.-H. Chen, J.T. Yang, H.M. Martinez, Determination of the secondary structures of proteins by circular dichroism and optical rotatory dispersion, *Biochemistry* 11 (1972) 4120–4131.
- [63] F. Ding, W. Liu, Y. Li, L. Zhang, Y. Sun, Determining the binding affinity and binding site of bensulfuron-methyl to human serum albumin by quenching of the intrinsic tryptophan fluorescence, *J. Lumin.* 130 (2010) 2013–2021.
- [64] S.M. Kelly, T.J. Jess, N.C. Price, How to study proteins by circular dichroism, *Biochim. Biophys. Acta Proteins Proteomics* 1751 (2005) 119–139.
- [65] M.J. Murray, M.J. Snowden, The preparation, characterisation and applications of colloidal microgels, *Adv. Colloid Interf. Sci.* 54 (1995) 73–91.